

See discussions, stats, and author profiles for this publication at: <https://www.researchgate.net/publication/4693311>

# The Structure and Dynamics of Bubble-Type Vortex Breakdown

**Article** in *Proceedings of The Royal Society A Mathematical Physical and Engineering Sciences* · February 1990

DOI: 10.1098/rspa.1990.0076 · Source: NTRS

CITATIONS

57

READS

77

3 authors:



**Robert Spall**

Utah State University

89 PUBLICATIONS 983 CITATIONS

[SEE PROFILE](#)



**Robert Ash**

Old Dominion University

117 PUBLICATIONS 856 CITATIONS

[SEE PROFILE](#)



**T. B. Gatski**

208 PUBLICATIONS 6,318 CITATIONS

[SEE PROFILE](#)

Some of the authors of this publication are also working on these related projects:



Temporal Large-Eddy Simulation (TLES) [View project](#)

## The structure and dynamics of bubble-type vortex breakdown

By R. E. SPALL<sup>1</sup>†, T. B. GATSKI<sup>2</sup> AND R. L. ASH<sup>1</sup>

<sup>1</sup> *Department of Mechanical Engineering and Mechanics, Old Dominion University,  
Norfolk, Virginia 23509-0247, U.S.A.*

<sup>2</sup> *Viscous Flow Branch, NASA Langley Research Center, Hampton,  
Virginia 23665-5225, U.S.A.*

*(Communicated by M. Gaster, F.R.S. – Received 20 October 1989)*

[Plate 1]

A unique discrete form of the Navier–Stokes equations for unsteady, three-dimensional, incompressible flow has been used to study vortex breakdown numerically. A Burgers-type vortex was introduced along the central axis of the computational domain, and allowed to evolve in space and time. By varying the strength of the vortex and the free stream axial velocity distribution, using a previously developed Rossby number criterion as a guide, the location and size of the vortex breakdown region was controlled. While the boundaries of the vortex breakdown bubble appear to be nominally symmetric, the internal flow field is not. Consequently, the mechanisms for mixing and entrainment required to sustain the bubble region are different from those suggested by earlier axisymmetric models. Results presented in this study, for a Reynolds number of 200, are in good qualitative agreement with higher Reynolds number experimental observations, and a variety of plots have been presented to help illuminate the fluid physics.

### 1. INTRODUCTION

Prediction of vortex breakdown has important applications in aerodynamics and combustion. For instance, the occurrence of vortex breakdown over delta-winged aircraft alters the wing's lift and drag characteristics significantly. Tip vortices shed from large aircraft impose constraints on the frequency of take-offs and landings at major airports. Solutions to problems of this type require a knowledge of the conditions favourable to the occurrence of breakdown, but a detailed knowledge of the internal structure of the breakdown is unimportant. Other applications, however, require a knowledge of the internal structure. An example is swirl combustors, where swirling flows are used to stabilize high-intensity combustion processes (Syred & Beer 1974). Here the breakdown region acts to stabilize combustion by recirculating hot gases around the base of the flame. Quantitative experimental measurements are sparse and unsteady three-dimensional numerical studies are conspicuously absent due to complexity and cost. However, the breakdown process can only be understood as an unsteady,

† Present address: High Technology Corporation, P.O. Box 7262, Hampton, Virginia 23666, U.S.A.

three-dimensional flow. The present investigation has studied vortex breakdown using a fully three-dimensional, unsteady numerical simulation for the purpose of identifying the important flow processes which occur within a breakdown bubble. While the investigation cannot address all aspects of the breakdown process, we have been able to identify important structural and dynamic features.

Theories due to Squire (1960), Benjamin (1962), Gartshore (1962), Hall (1967) and Mager (1972) attempted to define conditions under which breakdown was likely to occur without attempting to predict the internal structure. Squire (1960) introduced the useful concept of a critical condition. By choosing certain functional forms for the base vortex flow, the nonlinear equations of motion (inviscid, steady) were reduced to a linear disturbance equation. He subsequently solved the equation to determine conditions under which a steady perturbation to the flow could exist. This condition, in terms of a swirl ratio, was taken as the condition for which vortex breakdown occurred. Benjamin (1962) examined this phenomena from a different point of view. He considered vortex breakdown to be a finite transition between two dynamically conjugate states of flow, similar to the occurrence of a hydraulic jump in open channel flow. The two states were a subcritical state, which was defined as a flow which could support standing waves, and a conjugate supercritical state, which was defined as a flow that was unable to support standing waves. In this context, the work of Squire defined a condition marking the interface between the two states. As a result, Benjamin (1962) and Squire (1960), although starting from different perspectives, arrived at the same criticality condition for similar types of vortex flows.

Another school of thought involves the similarity of the vortex breakdown phenomena to boundary layer separation or flow stagnation (Gartshore 1962; Hall 1967). Stuart (1987) has attempted to show that the concepts of flow stagnation and a critical state can be used to describe vortex breakdown in a complementary fashion.

Theories which attempt to give detailed information regarding the internal structure of the breakdown have been put forth by Bossel (1969), Randall & Leibovich (1973) and Ito *et al.* (1985). In the inviscid work of Ito *et al.* (1985), streamlines corresponding to different combinations of disturbances in the azimuthal direction were shown. These streamlines had the appearance of the different types of vortex breakdown observed experimentally.

Experimental work on vortex breakdown has been carried out principally for swirling flows in straight or slightly diverging tubes (Sarpkaya 1971*a, b*, 1974; Faler & Leibovich 1977, 1978; Garg & Leibovich 1979; Escudier & Zhender 1982; Uchida *et al.* 1985). Faler & Leibovich (1978) and Uchida *et al.* (1985) presented laser Doppler velocimeter measurements of the internal structure of bubble-type vortex breakdown flow fields. The time-averaged streamlines determined by Faler & Leibovich revealed a two-celled internal structure. They showed that the recirculation zone was 'dominated by energetic, non-axisymmetric, low-frequency periodic fluctuations'. Similar observations were made in flow visualization studies by Sarpkaya (1971*a*).

Numerical solutions of the steady and unsteady axisymmetric Navier-Stokes equations for vortex breakdown have been obtained by Lavan *et al.* (1969), Kopecky & Torrance (1973), Grabowski & Berger (1976), Narin (1977), Krause

*et al.* (1983), Benay (1984) and Hafez *et al.* (1986). In all cases, solutions were obtained which exhibited some of the characteristics observed experimentally in vortex breakdown. Krause *et al.* (1983) were the only investigators whose numerical solutions produced a two-cell internal structure. However, their solutions appeared to be distorted by the limited size of the computational domain and for some of the time levels, the breakdown bubble lifted off the axis. The other numerical solutions did not predict a two-cell structure and tended toward a steady state. Furthermore, when breakdown occurred, it invariably did so at the inflow boundary. This problem has been discussed in some detail by Leibovich (1978) and Spall *et al.* (1987).

The inflow boundary condition effect has been demonstrated by Spall & Gatski (1987) using the same numerical approach as the present investigation. Their results showed that for flows where breakdown was simulated near the inflow boundary, the breakdown bubble was symmetric, stable and single-celled. Since a rectangular grid was also employed in that numerical study, they showed simultaneously that their computational method could accommodate steady, axisymmetric solutions. In fact, their results were consistent with previous numerical studies. However, the authors went to some length discussing their scepticism regarding the validity of the predicted flow.

In the present study, the Navier–Stokes equations were solved using the velocity–vorticity formulation of Gatski *et al.* (1989). The formulation is briefly outlined and discussed in §2.1. The initial and boundary conditions are formulated in §2.2 and the results are discussed in §3. The flow structure of the bubble was studied using planar projected velocity vectors as well as particle traces and vortex lines. These kinematic descriptors were obtained using PLOT3D, a three-dimensional colour graphics program implemented on an IRIS workstation. These numerical results are compared qualitatively to the experimental results of Faler & Leibovich (1978). Further analyses of the bubble motion is performed using velocity profiles at axial stations upstream, within, and downstream of the bubble. In order to analyse the dynamics of the breakdown process, contour plots of axial velocity, vorticity, and pressure are shown. In addition, the rates of change of integrated total energy and enstrophy are presented and plotted as a function of axial location.

## 2. DIFFERENTIAL AND NUMERICAL FORMULATION

### 2.1. Governing equations and numerical algorithm

We consider in this study the full three-dimensional unsteady, incompressible, vortical flow of a newtonian fluid in an unbounded domain. The relevant non-dimensional governing equations, in terms of the velocity,  $\mathbf{u} = \mathbf{u}(\mathbf{x}, t)$ , and vorticity,  $\boldsymbol{\zeta} = \boldsymbol{\zeta}(\mathbf{x}, t)$ , variables, are given by

$$\nabla \cdot \mathbf{u} = 0, \quad (1a)$$

$$\nabla \times \mathbf{u} = Ro^{-1} \boldsymbol{\zeta}, \quad (1b)$$

$$D\boldsymbol{\zeta}/Dt = \partial\boldsymbol{\zeta}/\partial t + (\mathbf{u} \cdot \nabla) \boldsymbol{\zeta} = (\boldsymbol{\zeta} \cdot \nabla) \mathbf{u} + Re^{-1} \nabla^2 \boldsymbol{\zeta}, \quad (2a)$$

$$\text{and from (1b),} \quad \nabla \cdot \boldsymbol{\zeta} = 0. \quad (2b)$$

Both the Reynolds number,  $Re$ , and Rossby number,  $Ro$ , appear explicitly in this formulation. The Reynolds number ( $\equiv U^*r^*/\nu$ ) is based on a characteristic axial velocity,  $U^*$ , a characteristic viscous lengthscale,  $r^*$ , and the kinematic viscosity,  $\nu$ . In the present context, this lengthscale is also associated with the characteristic core radius of the initial axisymmetric longitudinal vortex. The Rossby number ( $\equiv U^*/r^*\Omega$ ) is also based on the characteristic axial velocity and core radius as well as a characteristic vortex core rotation rate,  $\Omega$ . Thus this Rossby number is similar to the ratio of a characteristic axial velocity to a characteristic swirl velocity. The above definition of the Rossby number implies that the characteristic velocity scale is defined with respect to a frame of reference in which the vortex breakdown bubble is stationary. Specification of  $U^*$ ,  $r^*$  and  $\Omega$  are developed from the prescribed initial conditions for the flow and will be discussed in the next section.

The Rossby number appears in a slightly non-standard way in (1) and (2). This is due to the scaling of the time variable,  $t$ , in the transport equation by the inertial scale,  $U^*/r^*$ , rather than the characteristic rotation rate,  $\Omega$ . Scaling the time variable with  $\Omega$  would simply result in a modified timescale appearing in (2); that is, a non-dimensional time multiplied by  $Ro$ . The present form of (1) and (2) allows one, however, to control  $Re$  and  $Ro$  independently. As has been shown by Spall *et al.* (1987), and as has been utilized in the present study, the Rossby-number-Reynolds-number parameter basis plays a crucial role in the initiation of the breakdown process.

The numerical algorithm used in this study is based upon a compact method developed by Gatski *et al.* (1989) (hereinafter referenced as GGR), to solve (1) and (2). We consider the cartesian coordinate system  $\mathbf{x} = (x, y, z)$  on which the computational domain is subdivided using irregularly sized volume elements. We define the dependent variables  $\mathbf{u}$  and  $\boldsymbol{\zeta}$  to have components  $(u, v, w)$  and  $(\zeta_x, \zeta_y, \zeta_z)$  respectively.

A typical cartesian element,  $e$ , is shown in figure 1 centred at  $(i, j, k)$ ; that is,  $e_{i,j,k}$ . The velocity variables are defined at the edge of the element and the vorticity components are defined at the centre of faces of the element. In the actual implementation of the scheme, velocity variables are constructed from box-variables (Keller 1970) defined at the vertices of the element.

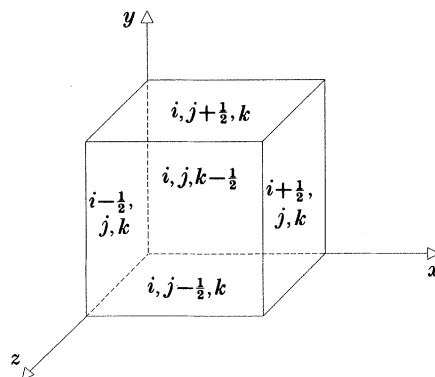


FIGURE 1. Cartesian element,  $e$ , with centre at  $(i, j, k)$ .

The algorithm as applied to (1) and (2) is a five-step procedure within a time strip  $S^m$  of size  $\Delta t$  and consisting of: (i) given an initial condition (or iterative guess) solve (1a, b) subject to appropriate velocity boundary conditions and compatibility requirements on  $\zeta$  (see (iv)); (ii) construct boundary conditions for the vorticity field from previous vorticity values (in  $S^{m-1}$ ) and/or velocity field from (i); (iii) with boundary conditions from (ii) and velocity field from (i), as well as an initial condition (or iterative guess) solve for the vector field  $\zeta$ ; (iv) since there is no explicit requirement that the resultant field is solenoidal, and this is a required condition on the vorticity field  $\zeta$  for (i), construct a solenoidal field from  $\zeta$  using a Helmholtz decomposition; (v) proceed to step (i) and repeat the process within the time strip  $S^m$  until a predetermined convergence criterion is met.

The kinematic velocity equations, (1a) and (1b), must be solved subject to the direct specification of one velocity component on each face of the boundary surface,  $\Gamma$ , of domain  $D$  (see GGR and cf. Wu 1984). The remaining velocity boundary conditions must be applied in step (ii) in the determination of the vorticity boundary conditions. In this vorticity boundary condition specification, the velocities are used either directly, that is through an application of (1b) and appropriate one-sided differences, or indirectly, through an application of appropriate flux conditions (see §2.2). In either case all vorticity components on the boundary surfaces need to be specified, and this specification must satisfy the requirement that  $\int \zeta \cdot \mathbf{n} d\Gamma = 0$ .

To complete the discussion of the differential and numerical problem it is necessary to examine the governing equation for the pressure field,  $P$ . Note that the pressure field is an artefact of the computation rather than an integral part of the solution method. A Poisson equation for the pressure is easily derived from the momentum equation and is given here in the form

$$\nabla^2 P = f(\mathbf{u}, \zeta), \quad (3a)$$

$$\text{where} \quad f(\mathbf{u}, \zeta) = \nabla \cdot [\mathbf{u} \times \zeta - \nabla(\tfrac{1}{2}\mathbf{u} \cdot \mathbf{u})]. \quad (3b)$$

This equation is solved using the same numerical scheme developed for the projection of the vorticity field. For the pressure Poisson equation, the Neumann boundary conditions are extracted from the momentum equations, i.e.

$$\nabla P = \mathbf{u} \times \zeta - Re^{-1}(\nabla \times \zeta) - \mathbf{u}_t \quad \text{on } \Gamma. \quad (4)$$

The right-hand side of (4) is evaluated using the boundary values for the velocity and vorticity and, where necessary, one-sided difference approximations to the required derivatives are used. In addition, Green's theorem applied to (3a) yields the compatibility condition

$$\int f(\mathbf{u}, \zeta) dV' = \oint \mathbf{n} \cdot \nabla P d\Gamma', \quad (5)$$

where  $\int dV'$  indicate the integration is over the whole domain. This condition is enforced explicitly through the pressure gradient boundary conditions.

## 2.2. Initial and boundary condition specification

The intent of the present study was to analyse the evolution of a model vortex representative of the roll-up of a trailing sheet vortex from a wing. Observations

have revealed that unconfined vortices such as these are nominally axisymmetric with an appreciable axial velocity excess or deficit relative to the free stream, depending on the wing loading. In addition, far downstream of the wing, the flow outside of the core is nearly irrotational.

Experimental measurements of a trailing wing tip vortex (Singh & Uberoi 1976) and vortices produced in a tube and vane apparatus (Faler & Leibovich 1978) revealed that the circumferential velocity profile was well represented by the two-dimensional Burgers vortex. The axial velocity appeared to decay exponentially in the radial direction (from the vortex centreline), reaching a constant value at large radius. These observations lead to the following dimensional form for the swirl and axial velocity profiles (see Lugt 1983; Spall 1987; Faler & Leibovich 1978).

$$V_\theta = K/r(1 - \exp[-ar^2/2\nu]), \quad (6)$$

$$U = U_\infty + U_0 \exp[-ar^2/2\nu]. \quad (7)$$

Here,  $K$  is a constant, which is proportional to the circulation, and  $a$  is an adjustable constant associated with the vortex core diameter.  $U_\infty$  is the freestream axial velocity and  $U_0$  is an axial velocity excess (or deficit) occurring at the vortex centreline. Profiles similar to these were used in numerical studies of vortex breakdown by Kopecky & Torrance (1973) and Benay (1984). In these studies, as in the present study, the initial radial velocity was assumed equal to zero.

In the above equations, and the equations of motion in §2.1, length is non-dimensionalized by  $r^*$ , where  $r^* = \sqrt{(2\nu/a)}$ . Velocities are non-dimensionalized by the axial velocity,  $U^*$ , occurring at the radius  $r^*$ , and vorticities are non-dimensionalized by  $\Omega$ , defined as the solid body rotation rate obtained from  $\Omega = \lim_{r \rightarrow 0}(V_\theta/r) = aK/2\nu$ .

The non-dimensional forms of (6) and (7) become

$$v_\theta = Ro^{-1}(1 - e^{-r^2})/r, \quad (8)$$

$$u = (1 + \beta e^{-r^2})/(1 + \beta e^{-1}), \quad (9)$$

where  $\beta = U_0/U_\infty$ . The non-dimensional axial component of vorticity, for the velocity distribution given by (8) and (9), is given by

$$\zeta_x = 2e^{-r^2}. \quad (10)$$

These expressions, (8)–(10), represent the form of the vortex used in the present study from which the initial and boundary conditions are derived. The initial vortical distribution was cylindrical (i.e. no variations in the axial direction and no radial velocities). The vortex was aligned along the  $x$ -axis and the rotation was such that the axial component of vorticity was positive. The boundary conditions at inflow are discussed first, followed by the outflow conditions and conditions on the lateral boundaries.

The numerical solution for the velocity equations requires the specification of a single component of the velocity vector on the boundaries. The discretized form of the transport equation for  $\zeta$  (see GGR) requires the specification of three components of  $\zeta$  on the boundaries. For the numerical implementation of the boundary conditions, the above equations (8)–(10) are expressed in terms of cartesian coordinates.

At the inflow plane a uniform axial velocity profile was assumed; that is, (9), with  $\beta = 0.0$ . The three components of vorticity are specified as

$$\zeta_x = 2 \exp \{ -[(y - y_c)^2 + (z - z_c)^2] \}, \quad (11)$$

$$\zeta_y = Ro(\partial u / \partial z - \partial w / \partial x), \quad (12)$$

$$\zeta_z = Ro(\partial v / \partial x - \partial u / \partial y). \quad (13)$$

Here  $\partial u / \partial z$  and  $\partial u / \partial y$  are zero from (9) and the terms  $\partial w / \partial x$  and  $\partial v / \partial x$  are obtained using forward finite-difference approximations.

The velocity boundary condition at the outflow boundary is chosen to satisfy

$$\partial v / \partial y + \partial w / \partial z = \text{const.} \quad (14)$$

This is a statement relating the divergence of the velocity in the plane perpendicular to the vortex axis to the acceleration of the axial velocity. Flux conditions are chosen for the vorticity boundary conditions. Here, the effects of viscosity are neglected and the Dirichlet-type boundary conditions are obtained from

$$D\zeta/Dt = \zeta \cdot \nabla \mathbf{u}. \quad (15)$$

The known velocities and vorticities in (15) are taken at time level  $m$ . The time derivative is discretized using forward differences. The resulting discretized equation is then solved for the vorticity vector at time level  $m + 1$ .

Based on the problems described by Spall & Gatski (1987), it was necessary to use a lateral boundary condition which could be used to control the location of vortex breakdown. To that end, an axial velocity was specified on the lateral boundaries. Previously, Hall (1967) used a prescribed pressure distribution on the lateral boundaries for the parabolic problem. Alternatively, using the recent results of Spall *et al.* (1987) which identified a Rossby number criterion for predicting vortex breakdown, it is possible to justify an axial velocity boundary condition for the purpose of controlling the breakdown location. At Reynolds numbers greater than 100, vortex breakdown occurs at a local Rossby number of approximately 0.7. By using an inflow boundary condition with a minimum local Rossby number which is supercritical, breakdown can be delayed in a spatial sense. A supercritical value of 0.9 was used in this study and the axial velocity distribution on the lateral boundaries was then adjusted to decelerate the flow, causing the local Rossby number to decrease below the critical value.

The Reynolds number was also controlled. Since the critical Rossby number is nominally constant at Reynolds numbers greater than 100, a Reynolds number of 200 was chosen. This moderate value provides a flow which is relatively insensitive to Reynolds number effects, but which does not demand the finer computational mesh which becomes prohibitive at high Reynolds numbers.

A linear deceleration of the free-stream axial velocity was specified:  $u = 1.0$ ,  $0 \leq x \leq 1.42$ ;  $u = 1.0 - 0.45((x - 1.42)/(16.0 - 1.42))$ ,  $1.42 \leq x \leq 16.0$ . The value  $x = 1.42$  corresponds to a grid point near the inflow boundary and the value  $x = 16.0$  corresponds to the length of the domain. This form was chosen due to its simplicity rather than for its relevance to a particular physical situation. Note that the 'constant' referred to in (14) is determined from the above specified deceleration. This decelerating free stream can be thought of as originating from



some source far from the vortex core. We are interested in the effect that this free stream potential flow has on the viscous core of the vortex. In this context, the above boundary conditions are representative of an unconfined vortex.

At the lateral boundaries ( $y = 0, 14$ ;  $z = 0, 14$ ), the initial value of the axial component of vorticity was set equal to the value given by (10). In addition, for a uniform axial velocity profile,  $\zeta_y = 0.0$  and  $\zeta_z = 0.0$ . The lateral boundaries were placed far enough from the vortex core so that the subsequent development of the breakdown did not alter the irrotational flow at these boundaries. Vorticity and velocity contour plots in the  $y$ - $z$  plane were used to monitor the far-field behaviour of these variables. Thus these conditions represented both the initial and boundary conditions for vorticity along the lateral boundaries.

The discretized form of the governing equations were solved over a  $73 \times 50 \times 50$  grid (72 cells in the  $x$ -direction, 49 cells in the  $y$ -direction, 49 cells in the  $z$ -direction). The domain was bounded by  $0 \leq y \leq 14$ ,  $0 \leq z \leq 14$ , and  $0 \leq x \leq 16$ . The vortex was positioned in the  $y$ - $z$  plane so that the initial vortex centreline was at  $y_c = 7.0$  and  $z_c = 7.0$ . Since the difference scheme is compact, grid clustering was easily performed. Grid points were clustered in regions where large gradients occurred. This included the region immediately upstream of the breakdown and the vortex core region. The  $y$ - and  $z$ -direction grid points (perpendicular to the vortex axis) were clustered near the vortex centreline and the  $x$ -direction grid points were clustered near the forward section of the domain.

Finally, since the numerical algorithm is implicit, there are no numerical constraints on the size of the time step,  $\Delta t$ . However, implied constraints, such as requiring the numerical time step to be less than the (minimum) characteristic timescale associated with the velocity gradient field (see (4)) or applying the usual CFL condition, are necessary for temporally accurate solutions. Based on these constraints, a  $\Delta t$  value of 0.1 was used throughout the simulation.

### 3. RESULTS AND DISCUSSION

Experimental measurements of quantities such as vorticity and pressure within the breakdown region are virtually unobtainable. Other quantities, such as stress or strain rate fields, are also difficult if not impossible to obtain. For applications dependent on the structure and dynamics of the breakdown recirculation region, a knowledge of these quantities is invaluable for optimal control and efficient utilization. Therefore, the results presented in this section will, hopefully, add to an understanding of vortex breakdown.

As has been shown earlier in this paper, there are two relevant controlling parameters: the Rossby number and the Reynolds number. The results presented in this section were obtained at a Rossby number of 0.90 and a Reynolds number of 200, coupled with the initial and boundary conditions discussed in the previous section. Note that these parameter values are not local values but fixed values based on characteristic scales at inflow. The simulation required about 80 time units before the breakdown bubble became fully sized and internally well developed within the computational domain. It is natural to inquire as to the effects of increasing Reynolds number on vortex breakdown. We have performed

some computations for  $Re = 1000$ , and present these preliminary results at the end of this section.

To get a pictorial representation of the overall bubble structure and dynamics, it is instructive to examine a time sequence of planar projected velocity vectors. Figure 2*a-e* shows this sequence covering a time span of exactly 30 units. The view shown is in the  $x$ - $y$  plane at a  $z$ -axis location corresponding to the initial vortex centreline, i.e.  $z = z_c = 7.0$ . Note that the entire domain is not shown, just the relevant bubble breakdown area. As is seen, the gross exterior appearance of the bubble is axisymmetric while the internal structure is clearly asymmetric. At time  $t = 85.0$  the internal structure of the breakdown contains two major cells, or vortex rings, rotating in opposite directions about their respective core axes. The

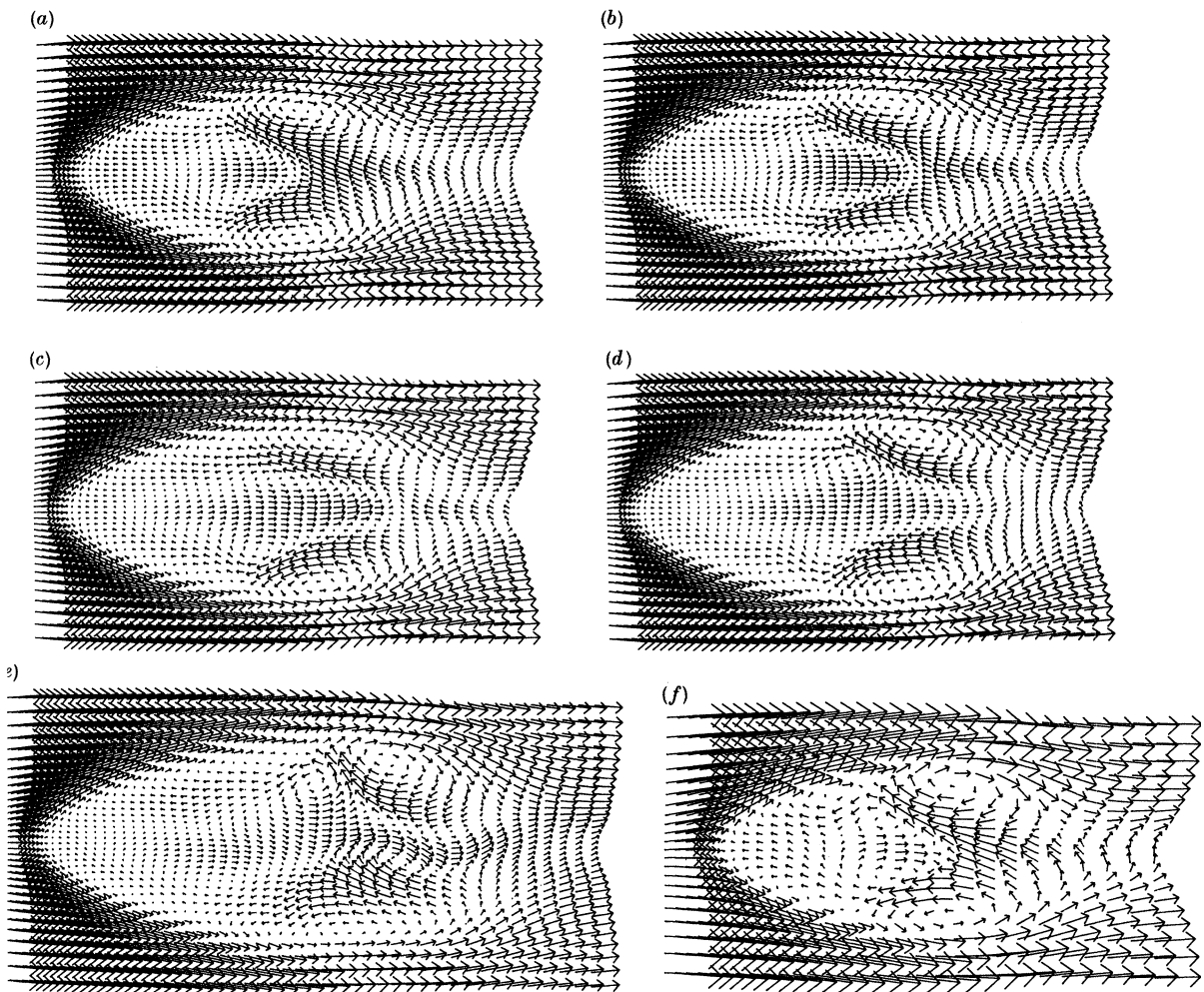


FIGURE 2. Planar projected velocity vectors over the interior of the breakdown region at different time levels. (a)  $t = 85$ , (b)  $t = 90$ , (c)  $t = 95$ , (d)  $t = 100$ , (e)  $t = 115.0$ ; ((f)  $t = 90.0$  ( $48 \times 34 \times 34$  grid)).

fluid enters the bubble from the downstream end and is drawn into the lower portion of the aft vortex ring. The exchange of fluid between the fore and aft rings appears minimal, although some fluid is convected into the forward portion of the bubble. This exchange takes place near the outer region of the bubble approximately  $0.4L$  units downstream from the front stagnation point (where  $L$  is the length of the bubble). It does not appear that the fluid which has entered the forward section of the bubble re-enters the aft section. The fluid exits the bubble from the outer edges of the forward section and via the aft vortex rings. This fluid then follows the outer envelope of the bubble with a certain amount from the aft vortex ring re-entering, and the remainder being convected downstream. In addition, the velocities are considerably greater in the aft portion of the bubble than in the forward portion. The length-to-diameter ratio of the bubble is approximately 1.75 with the maximum diameter occurring approximately  $0.7L$  units downstream from the front stagnation point. From the above discussion, it is clear that the dominant means of momentum transfer is convection and not diffusion.

The sequence of velocity vector plots for time levels  $t = 85$  to  $t = 115$  (figure 2*a-e*) reveals that the overall shape of the bubble does not change significantly with time. It is the interior structure of the bubble that shows a significant time dependence. A jetlike structure is seen to form along the axis of the bubble as it evolves in time. At  $t = 115$  the jet has penetrated the aft section of the bubble. The emergence of the jet appears to have affected the temporal stability of the flow on the aft portion of the bubble. A highly asymmetric region can be observed, although the major aft recirculation cells remain intact. In addition, the two forward cells remain, but again, considerable symmetry has been lost. An additional (fifth) cell is located between the large aft cells. The solution was marched further in time but due to the emergence of this strong shear layer on the aft section of the bubble, the spatial accuracy of the calculations could not be guaranteed. Thus the results are not presented at later times. In any case, the calculations indicate the absence of a steady state.

For comparison purposes, mean streamline and axial velocity profiles constructed by Faler & Leibovich (1978) using experimentally measured data, are reproduced in figure 3. Although, Reynolds number and free-stream velocity distributions are different, the qualitative agreement between the experimental and computational flowfields (figure 2*a-e*) is excellent.

In addition, the velocity vectors at  $t = 90$  which were obtained from a computation using a coarser ( $48 \times 34 \times 34$ ) grid, are shown in figure 2*f*. All other flow parameters were unchanged. Based on the excellent agreement between the two computed flow fields, a  $73 \times 50 \times 50$  grid was considered sufficient to capture the large-scale structures existing within the breakdown bubble.

Relevant to the question of resolution, it was deemed necessary to determine what, if any, effect the rectangular domain imposes on the computation of such a cylindrical vortex. To investigate this, contour plots in the  $y-z$  plane, at the axial location corresponding to the approximate maximum bubble diameter ( $x = 7.5$ ), were examined. Two of these contours, representing axial velocity and axial vorticity, are shown in figures 4 and 5 respectively. By examining the axial

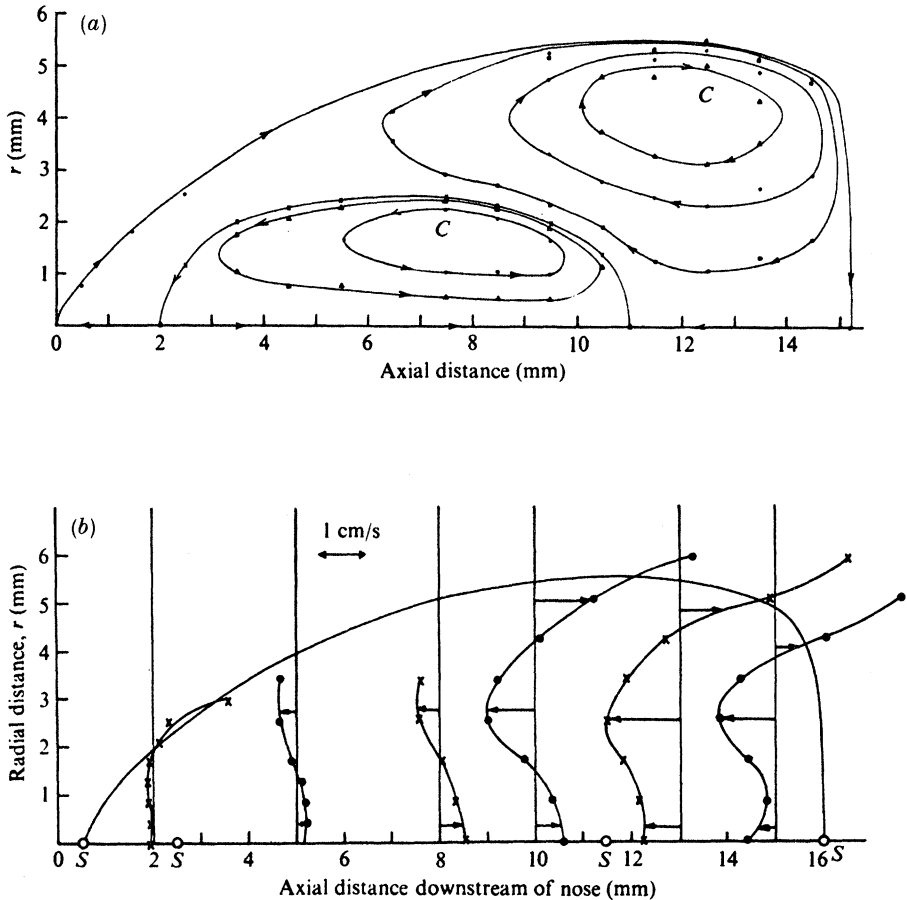


FIGURE 3. Experimentally determined mean streamline pattern and mean axial velocity profiles as measured by Faler & Leibovich (1978). (a) Experimental mean streamline pattern, (b) experimental mean axial velocity profile.

velocity contours, we note that the outermost contour level (0.80) appears completely unaffected by the presence of the boundary where the velocity is fixed at 0.81. The maximum contour level (1.0) indicates that fluid is accelerated around the outside of the bubble while the negative (dashed) contour lines represent regions of reversed flow within the bubble and place the size of the bubble in the perspective of the size of the computational domain. As additional evidence, the contours of axial vorticity shown in figure 5 indicate that the rectangular computational domain has no noticeable effect on the vortex. These results are consistent with the test cases run in GGR (1989).

The results of figure 2 are rather enticing, even though they are planar projected vectors. An analysis of other projection angles for viewing these vectors seemed to confuse rather than clarify the interpretation. However, additional insight can be gained by viewing the (instantaneous) particle paths extracted from the velocity field. Particle traces (at  $t = 95.0$ ) are displayed in figure 6*a*, plate 1. These

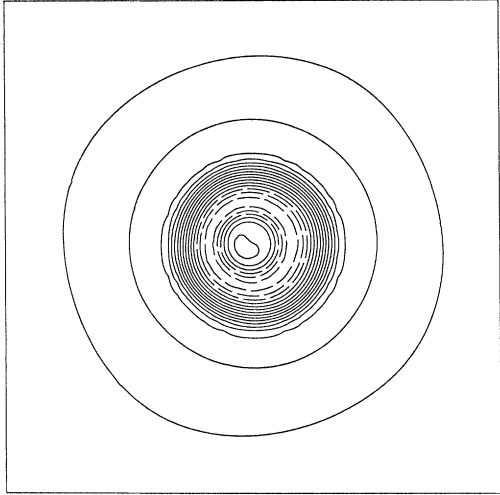


FIGURE 4. Contours of constant axial velocity. Contour levels range from  $-0.3$  to  $1.0$  in intervals of  $0.10$ .

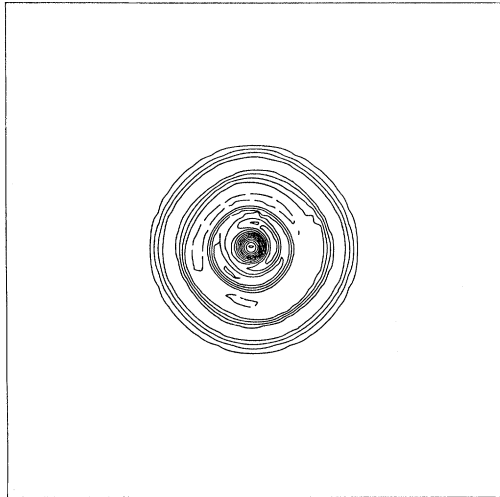
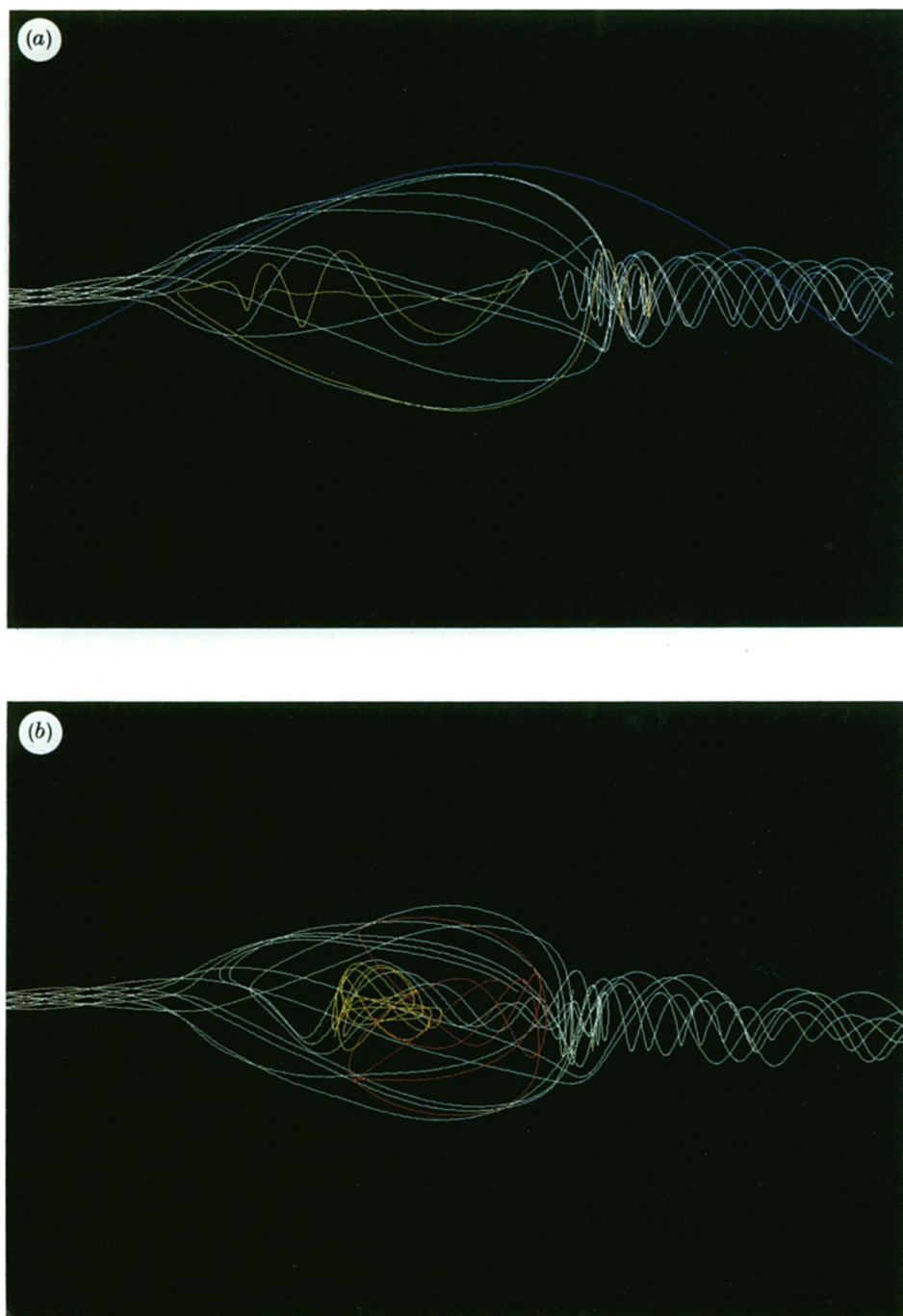


FIGURE 5. Contours of constant axial vorticity. Contour levels range from  $-0.1$  to  $1.2$  in intervals of  $0.1$  (zero level not shown).

trajectories satisfy the equations  $d\mathbf{x}/dt = \mathbf{u}(\mathbf{x}, t)$ . If a particle passes through the point  $(x_0, y_0, z_0)$  at time  $t = 0$ , the solution is of the form  $\mathbf{x} = \mathbf{x}(x_0, t)$  which traces out the pathline as  $t$  increases. However, the PLOT3D graphics package is limited to instantaneous particle traces and this factor must be considered when interpreting the traces. The nine white traces were generated from the inflow plane at radial positions within the rotational region of the vortex. A single blue trace was initiated at the inflow plane, but from a radial position in the irrotational region of the flow. The yellow trace was started from a position within the forward region of the breakdown bubble.



**FIGURE 6.** Particle path trajectories for flow with vortex breakdown; (a)  $t = 95$ , (b)  $t = 85$ .

The white traces appear to define the general shape of the breakdown bubble. The location where the white traces diverge corresponds to the position of the forward stagnation point. The yellow follows the path of the internal axial jet (see figure 2*c*) until a position is reached near the aft portion of the bubble. Here, the trace suggests that particles are convected to a radial position outside the jet, at which time a spiralling motion towards the front of the bubble ensues. The particle is then convected to the outer edge of the bubble, where it acts to define the bubble shape. The blue trace spirals about the breakdown bubble and is relatively unaffected.

In figure 6*b*, plate 1, traces are shown at  $t = 85$ . Again, a yellow trace was generated in the front portion of the bubble and, in addition, a red trace was generated from the aft section. The path of the yellow trace clearly reveals the small inner ring vortex (see figure 2*a*). This trace gets entangled within the vortex, eventually repeating its path. The red trace indicates the existence of the larger aft ring vortex. Clearly, information such as this is invaluable in understanding mixing applications which are dependent on the internal flow structure of the bubble.

It is also instructive to view instantaneous vortex lines (figure 7 at  $t = 95.0$ ). These are lines whose tangent is everywhere parallel to the vorticity vector. The lines are three-dimensional and are, once again, obtained using an IRIS colour graphics workstation and PLOT3D. The radial locations of these 16 lines at the inflow plane correspond approximately to the locations of the white particle traces at inflow in the previous figure. In the approach flow, the vortex lines are oriented in the  $x$ -direction, consistent with the inflow boundary conditions. The transfer of vorticity from the  $x$ - to the  $y$ - and  $z$ -components takes place as the first stagnation point is approached. Different orientations of the vorticity vector are observable within the bubble. Near the centreline of the bubble, the vorticity vector is oriented primarily in the axial direction. Near the outer regions, the orientation is mostly in the circumferential direction. Downstream of the breakdown, the vorticity vector is oriented in the axial direction, but with a superimposed small undulation. These observations will be expanded further when the vorticity contours are discussed.

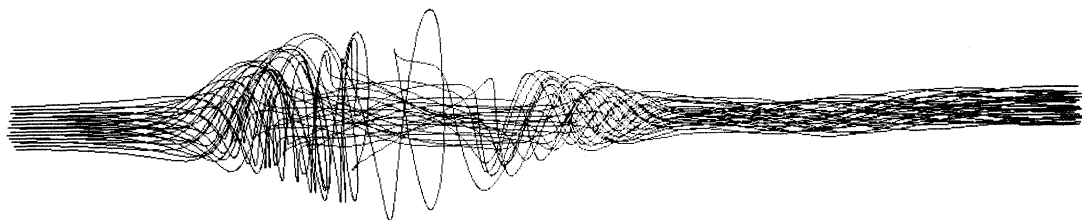


FIGURE 7. Vortex lines for flow with vortex breakdown.

As was outlined in the Introduction, there has been a long history of theoretical work in connection with vortex breakdown. Many of these studies have been based on the ideas of linear stability theory. Since this is a full simulation, the resultant

velocity profiles corresponding to the velocity vectors (e.g. figure 2*a*) are in fact total velocity profiles, that is in some sense a superposition of mean and perturbation profiles. Figure 8*a-d* show these 'total' velocity profiles at four different axial locations at time  $t = 95.0$ . Axial ( $x$ ), transverse ( $y$ ) and spanwise ( $z$ ) velocities are plotted as a function of the transverse coordinate (with a translation of the origin to the vortex centreline;  $y_c = 7.0$ ,  $z_c = 7.0$ ). Since the spanwise location of the data points is along the vortex centreline, the velocity components in a cartesian coordinate system are easily transformed to the corresponding components in a cylindrical system. The axial location of the profiles in figure 8*a* is upstream of breakdown ( $x = 0.45$ ). The profiles in figure 8*b* and *c* represent axial locations within the breakdown region ( $x = 4.43$  and  $x = 7.51$ , respectively). Profiles from downstream of the breakdown region are plotted in figure 8*d* ( $x = 13.97$ ). For reference purposes, the first stagnation point is located at  $x = 2.93$ . Upstream of breakdown, the spanwise (swirl) velocity profile approximates the two-dimensional Burgers vortex. The radial velocity is small and the axial velocity profile nearly uniform. Within the breakdown region, as revealed in figure

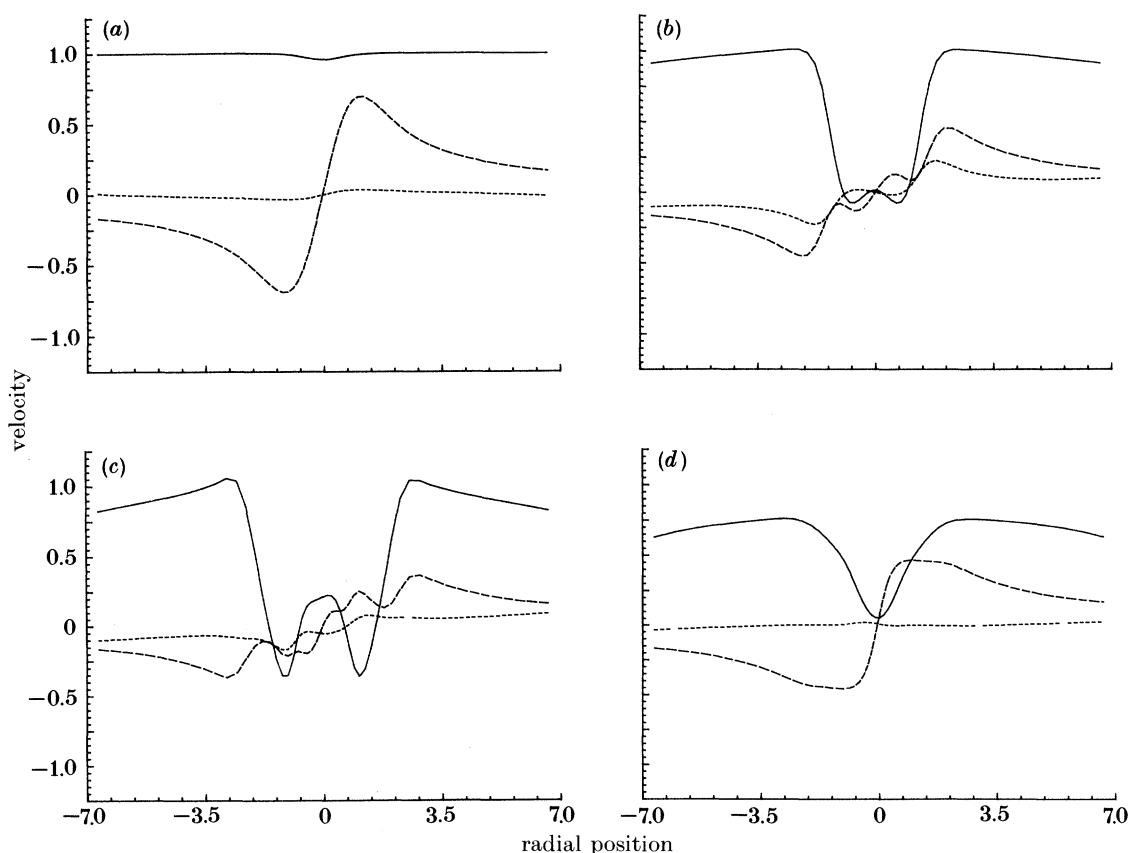


FIGURE 8. Transverse variation of axial, transverse (radial) and spanwise (swirl) velocity components at different axial locations. (a)  $x = 0.45$ , (b)  $x = 4.43$ , (c)  $x = 7.51$ , (d)  $x = 13.97$ . —, Axial velocity, ---, radial velocity; — · —, swirl velocity.



8*b* and *c*, the flow is no longer symmetric (cf. figure 2*a-e*). Transverse (radial) velocities are significant and the spanwise (swirl) velocity profiles no longer approximate Burgers vortex. At both axial locations within the breakdown, the axial velocity profiles have a local maximum and two local minima. The profiles in figure 8*d*, downstream of the breakdown region, reveal a large axial velocity deficit near the vortex centreline. This suggests that the axial velocity is much slower to relax back toward the pre-breakdown form relative to the other velocity components. The spanwise (swirl) velocity profiles reveal a solid body-like rotation near the centreline. At the edge of the core, however, the maximum spanwise (swirl) velocities are considerably less than those values occurring upstream of the breakdown region, and the characteristic radius of the vortex has decreased. In both the upstream and downstream locations, the magnitudes of the transverse (radial) velocities are small.

The spanwise (swirl) velocity profiles can be compared to those from Faler & Leibovich (1978) (their figs 12 and 13). Within the breakdown bubble, the swirl (spanwise) velocity results of figure 8*b* and *c* are qualitatively similar to those of fig. 13 in their study. Downstream of the breakdown bubble, the swirl (spanwise) velocity distributions seem to deviate between the two studies. The local characteristic rotation rate (see §2.2) in both studies does indeed increase relative to the characteristic rates upstream of the bubble (this rotation rate is easily extracted from their figs 12 and 13 by examining the slope of the swirl velocity profiles near the centreline). However, they found that the characteristic size of the downstream vortical flow increased, whereas it was found in this study to decrease. This apparent discrepancy can be reconciled by a closer analysis of their downstream results. Their fig. 13 shows two local maxima in the swirl velocity distribution for the data taken 24 mm downstream from the bubble nose. If one considers the local maxima nearest the centreline, then the characteristic size has in fact decreased. The second (higher) maxima which appears in fig. 13 of the Faler & Leibovich (1978) study does not appear in the results shown in figure 8*d* here. Although close examination of figure 8*d* does suggest the emergence of a second local maxima in the spanwise (swirl) velocity distribution. It is difficult to form a one-to-one correspondence between the two studies in this particular case since the swirl velocity is necessarily zero at the tube boundaries in the Faler & Leibovich (1978) study, whereas, no such restriction applies in the free field problem presented here. If, however, this is not the cause of the second (higher) maxima, then the cause may be due to the enhanced mixing in the tube since transitional flow conditions exist downstream of the breakdown bubble (see Leibovich 1978). In the laminar flow considered here, this enhanced mixing mechanism is not present, and, therefore, the second (higher) maximum may not be present. Of course, if it were practical to continue the calculation further downstream, such a maxima may exist.

Up to this point we have been examining the characteristic features of the overall structure of the breakdown bubble. This analysis has suggested that the controlling dynamics within the bubble are rather complex. To further map out this motion, we will now examine some contour plots of the velocity and vorticity.

As a prelude to the presentation of these and other contour plots, it is necessary

to format the pictorial representations. Unless otherwise noted, the contour plots are shown in the  $x$ - $y$  plane along the vortex centreline,  $z = z_c = 7.0$ . Solid contour lines denote positive values (including zero), and dashed lines denote contours with negative values. In addition, they encompass the entire computational domain and represent data obtained at time level  $t = 95$  (cf. figures 2c, 6, 7 and 8). This particular time-level was chosen as qualitatively representative of the internal bubble structure; with the added feature that the forward and aft bubble recirculation regions were rather well delineated.

Figure 9 is a contour plot of the axial component of velocity. The breakdown bubble is located in the middle of the computational domain. As has been discussed in detail by Leibovich (1978) and Spall *et al.* (1987), and alluded to in the Introduction, the location of the breakdown region in close proximity to the inflow boundary was one of the deficiencies of previous numerical studies. The location of the breakdown bubble is controlled, in this study, by the free field axial velocity boundary condition (see §2.2). Figure 9 clearly shows the effects of this external flow deceleration.

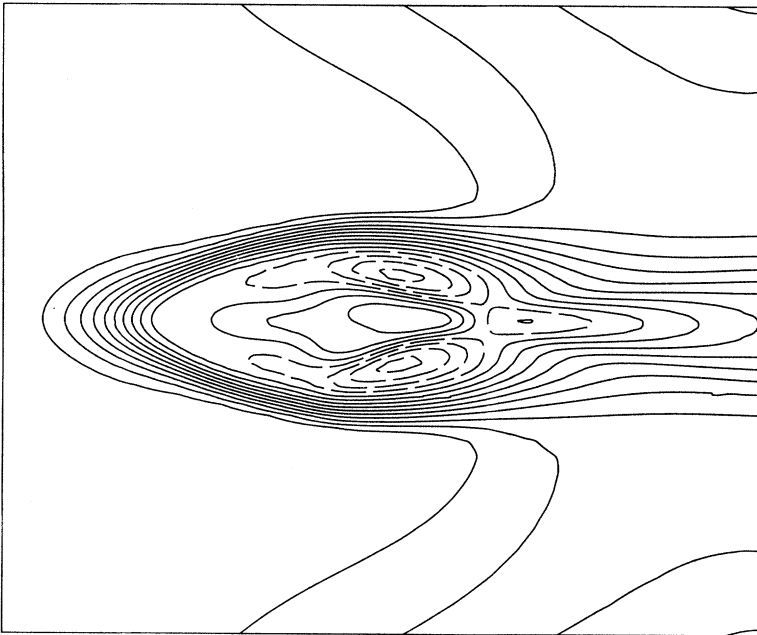


FIGURE 9. Contours of constant axial velocity. Contour levels range from  $-0.4$  to  $0.9$  in intervals of  $0.1$ .

In the interior of the bubble, the contours show a region of flow reversal, followed in the downstream direction by a region where the flow is again moving downstream, and then another flow reversal region. This region is terminated at the rear stagnation point, downstream of which the flow is unidirectional. Thus, within the breakdown bubble, there are four stagnation points along the bubble axis. This scenario suggests that there are intense normal and shear stress regions

(or strain rate regions) within the breakdown bubble. This is further substantiated by the velocity vector plot (figure 2c) and the particle trajectory plot (figure 6) discussed earlier. In particular, the abrupt directional changes shown in figure 6 suggest regions of intense acceleration (deceleration) within the bubble. Outside of the bubble, but in proximity to its boundary, the close spacing of the velocity contours suggest intense flow deceleration as the forward stagnation point is approached.

The strong accelerations and decelerations that were shown to occur within the breakdown bubble in figure 9 can be investigated further. This can be done by considering the rate of change of kinetic energy within the flow domain. The relevant equation for a cartesian system can be written as (see, for example, Batchelor 1967):

$$\frac{D}{Dt} \left\{ \int \left( \frac{1}{2} u_i u_i \right) dV' \right\} = - \int u_i \frac{\partial P}{\partial x_i} dV' + Re^{-1} \int u_i \frac{\partial^2 u_i}{\partial x_j \partial x_j} dV'. \quad (16)$$

The terms on the right-hand side of (16) contribute to the change of kinetic energy through pressure and viscous forces, respectively. The streamwise variation of the rate of change of kinetic energy is shown in figure 10. In order to get this pictorial representation, the volume integrals were evaluated at each of the 72 grid-cell locations, and over all grid cells in each corresponding  $y$ - $z$  plane. Because each 'planar' volume differs in size due to the variation of  $\Delta x$  in the downstream direction, it is necessary to normalize the integrated results at each  $x$ -station by the respective volume, i.e.  $196 \Delta x$  (recall from §2.2 that  $y_{\max} = z_{\max} = 14$ ). Thus the results presented in figure 10 need to be interpreted as rate of change of kinetic energy per unit volume. Figure 10 shows that the rate of change of energy due to pressure work is dominant. The contribution due to viscous work is small.

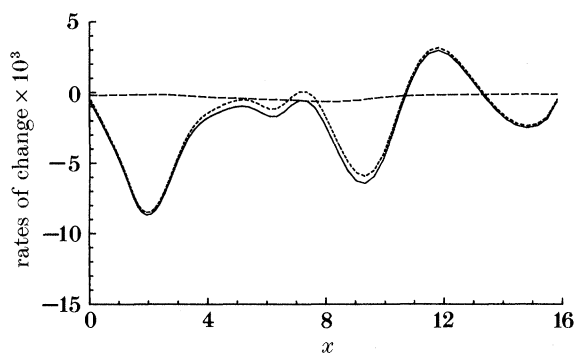


FIGURE 10. Variation of integrated rate of change of kinetic energy with axial location. ---, Pressure work; - · -, viscous work; —, kinetic energy.

Even though figure 9 is a plot of axial velocity contours and figure 10 represents rates of change of kinetic energy of a material volume of fluid, it is still possible to make a qualitative comparison of the two figures. This comparison between figures 9 and 10 reaffirms the analysis made earlier concerning the accelerating and decelerating characteristics of the flow in the breakdown bubble region. Figure 10

shows a strong flow deceleration down to  $x \approx 4.0$  and then, even with the imposed adverse pressure gradient in the free field, a region of near constant velocity from  $x = 4.0$  to  $x = 7.0$ . This region also appears in the contours of figure 9, where, internal to the breakdown bubble, positive axial velocity contours are embedded between negative contours. Towards the aft portion of the bubble, the flow is once again decelerated (see figure 10),  $7.0 \leq x \leq 10.5$ , and then accelerated  $10.5 \leq x \leq 13.0$ . This behaviour is also shown in figure 9, where a region of negative contours is embedded in the aft portion of the bubble between positive contour regions. Downstream of the bubble, the flow is once again accelerating.

It should be noted that it is difficult to obtain a meaningful time sequence of plots such as figure 10. This is due to the fact that in such a lagrangian analysis the volume integrals at each subsequent time must contain the same fluid elements; therefore, the initial integration volumes are distorted. This extension is beyond the intent of the analysis in this study.

Just as the results for the velocity field indicate that intense dynamic phenomena occur near and within the bubble, the vortex lines (figure 7) suggest the occurrence of intense vortical dynamics in this same region. Figure 11*a-c* shows the three components of vorticity  $\zeta_x$ ,  $\zeta_y$ , and  $\zeta_z$ , respectively, at  $z = z_c = 7.0$  and time  $t = 95.0$ . Note that figure 11*b*, which corresponds to the  $\zeta_y$  component, is shown in the  $x-z$  plane. The  $\zeta_y$  component in the  $x-y$  plane along the vortex centreline is approximately zero for the bubble-type breakdown shown. Thus a composite picture of the vortical structure in the  $x-y$  plane can be constructed from figure 11*a* and *c*, and figure 11*b* can be used to discern asymmetries.

Figure 11*a* shows that the inflow vorticity distribution is indeed symmetric (as specified) and that the outflow vorticity distribution is nearly so, although more intense. This means that, through vortex stretching, the breakdown bubble acts to intensify axial vorticity; that is, the magnitude increases and characteristic size decreases. (In the absence of internal sources or sinks and with the explicit enforcement of  $\nabla \cdot \zeta = 0$ , the total vorticity of the system is conserved.) This is consistent with the observation made earlier in connection with the analysis of the velocity profiles (cf. figure 8*a* and *d*; Faler & Leibovich (1978)). In figure 8*d*, the spanwise (swirl) velocity distribution downstream of the breakdown also showed magnitude intensification (based on local characteristic rotation rate) and reduction of characteristic size.

Within the breakdown bubble, the scenario changes and the level of axial vorticity is reduced. Due to vortex tilting, the vorticity has been redistributed to the other vorticity components. Figure 11*c* shows that near the outer edges of the breakdown bubble significant amounts of  $\zeta_z$  vorticity exist. Furthermore, in the centre and aft portion of the bubble, but off the centreline, the vorticity field is dominated by the  $\zeta_z$  component vorticity. Note, however, that the  $\zeta_z$  component does not dominate the entire interior region; there is still a region along the centreline where the influence of the  $\zeta_x$  component of vorticity is significant. An additional interesting observation is that the downstream 'tails' remained 'attached' to the main bubble structure. This may be explained by the lack of a background perturbation field in such a laminar flow computation.

As the results of figure 11 show, there is a significant amount of vorticity

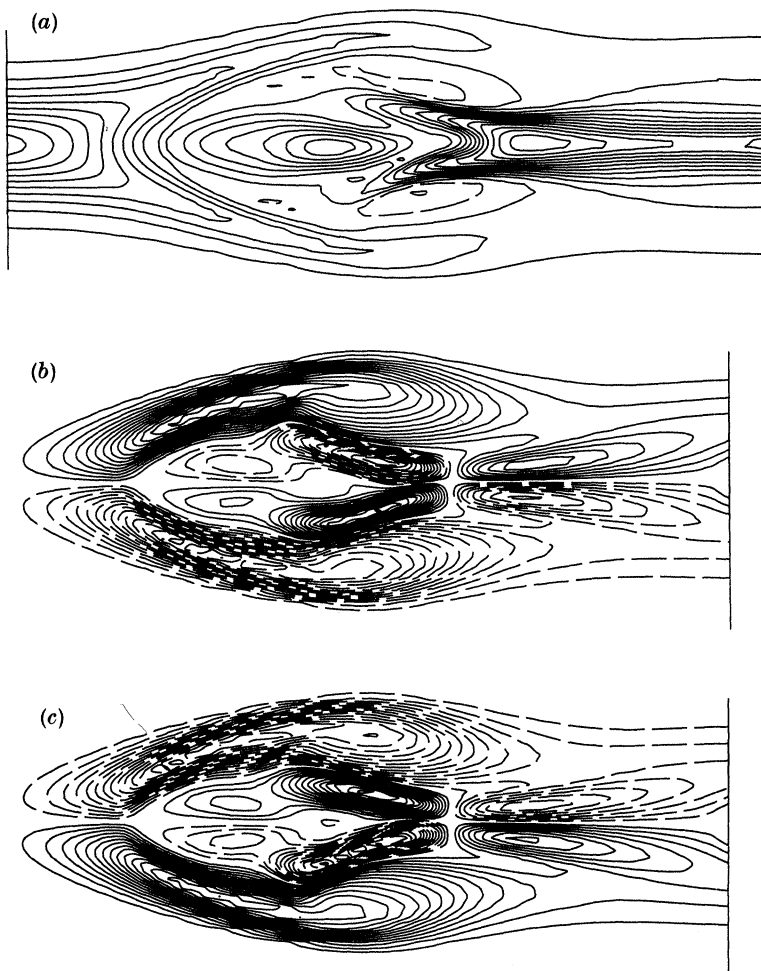


FIGURE 11. Contours of constant vorticity. (a)  $\zeta_x$  vorticity with contour levels ranging from  $-0.30$  to  $2.50$  in intervals of  $0.20$ ; (b)  $\zeta_y$  vorticity ( $x$ - $z$  plane) with contour levels ranging from  $-1.40$  to  $1.40$  in intervals of  $0.20$ ; (c)  $\zeta_z$  vorticity with contour levels ranging from  $-1.40$  to  $1.40$  in intervals of  $0.10$ .

redistribution among the components. It is also desirable to examine the rate of change of total vorticity. Analogous to the rate of change of total energy equation, (16), the rate of change of enstrophy can be written as (see, for example, Batchelor 1967):

$$\frac{D}{Dt} \left\{ \int \frac{1}{2} \zeta_i \zeta_i dV' \right\} = \int \zeta_i \zeta_j \frac{\partial u_i}{\partial x_j} dV' - Re^{-1} \int \left( \frac{\partial \zeta_i}{\partial x_j} \right)^2 dV' + \frac{1}{2} Re^{-1} \int \frac{\partial}{\partial x_j} (\zeta_i \zeta_i) n_j d\Gamma', \quad (17)$$

where  $n_j$  is the outward unit normal and  $\int d\Gamma'$  means integration around the boundary of  $V'$ . The right-hand side of (17) shows that the total amount of vorticity in a volume can change as a result of vortex stretching and viscous effects. The first term on the right, the stretching term, is positive if the fluid

element is extended in the direction of the local vortex lines, and negative if the fluid element is compressed. The second term shows that the effect of viscosity in the absence of diffusive transport across boundaries, is to decrease the total vorticity of the fluid. The third term represents diffusive transport across boundaries. Nevertheless, in some flow regions it is possible for the right-hand side of (17) to be positive, leading to local increases in the enstrophy.

The evaluation of the integrals in (17) were performed in the same manner as described for (16). Figure 12 shows the variation of rate of change of enstrophy as a function of downstream distance. From a lagrangian point of view the rate of change of enstrophy of a material volume (in this case of size  $196\Delta x$ ) is due to both temporal changes and spatial distortions of the volume. Since breakdown is an unsteady phenomena, the temporal changes may be significant. Whenever the rate of change of enstrophy is negative, the total amount of vorticity contained in a material volume passing through that location is decreasing. From figure 12 it can be seen that the distribution of enstrophy within the breakdown region is affected significantly by both vortex stretching and viscous action. The effect of viscosity is to offset the gains in enstrophy due to vortex stretching. The enstrophy changes due to diffusion across the boundaries of a specific material volume are very small. At first glance it appears that an inviscid calculation could model the essential physics within the breakdown bubble, since the spatial behaviour of the vortex-stretching term is similar to the spatial behaviour of the total rate of change. However, closer analysis raises the question of the effect and role of viscous forces in regions where the magnitude of the stretching term is small (e.g. at  $x = 8.5$ ). It may be that, to get the correct internal multicell structure, the inclusion of viscous effects is requisite. In comparing figure 11*a-c* with figure 12, it is seen that the location of the intense vortex ring structure coincides with the region where viscous effects dominate.

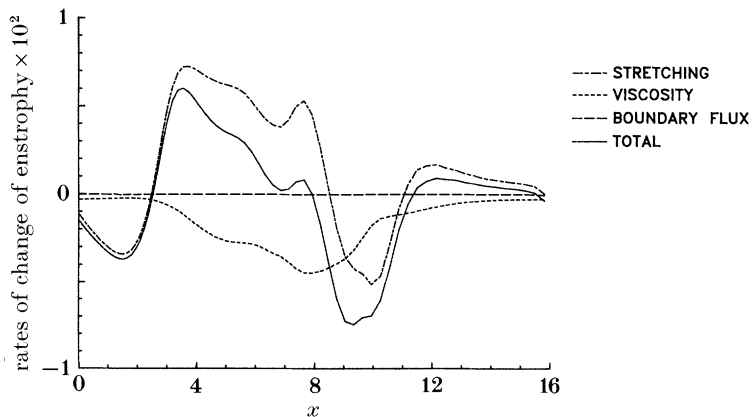


FIGURE 12. Variation of rate of change of integrated enstrophy with axial location.

In the present analysis the pressure is the only dynamic variable remaining to be examined. The Poisson equation for pressure was discussed in §2.1, and the solution of this equation yields the pressure contours shown in figure 13. Once

again, the contours shown are in the  $x$ - $y$  plane along the vortex centreline. The minimum pressure at an axial location occurs along the centreline of the vortex, with the absolute minimum ( $-0.5$ ) occurring at inflow. The maximum pressure contour in the figure, the  $0.0$  contour, is clearly shown as the only solid-line contour. Proceeding downstream from inflow, the contour levels increase until a local maximum is reached. This saddle-point region is located in the forward portion of the bubble and is distinguished by the short dashed contour lines ( $-0.02$ ,  $-0.03$ ,  $-0.04$ ,  $-0.05$ ,  $-0.06$ ,  $-0.07$ ,  $-0.08$ ,  $-0.09$ ). Thus the flow is decelerated by an adverse pressure gradient in the upstream region of the flow domain. In fact, both strong axial and transverse pressure gradients exist in this region.

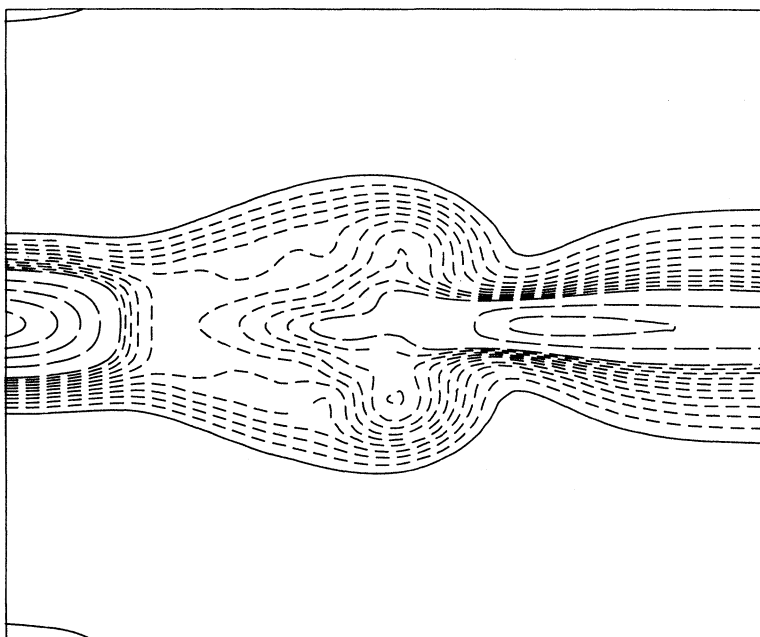


FIGURE 13. Isobar contours: contour levels of  $-0.5$  to  $0.0$ . Short dashed contour lines:  $-0.01$ ,  $-0.02$ ,  $-0.03$ ,  $-0.04$ ,  $-0.05$ ,  $-0.06$ ,  $-0.07$ ,  $-0.08$ ,  $-0.09$ . Other contours in intervals of  $-0.1$ .

Downstream of this saddle-point region the flow is again accelerated in the downstream direction. Another local minima ( $-0.3$ ) occurs along the vortex centreline at the aft end of the breakdown bubble, and this marks the end of the local flow acceleration field. Note that the pressure contours in this aft portion of the breakdown bubble are only slightly asymmetric.

It is possible to quantify the pressure gradients occurring in the vicinity of and within the bubble relative to the 'imposed' pressure gradient in the free field. The discussion in §2.2 on boundary conditions showed that an adverse pressure gradient was imposed through a linear deceleration of the free field axial velocity component. The resultant free-field pressure distribution is then computed from the Poisson equation for pressure. The axial pressure distribution along the  $y =$

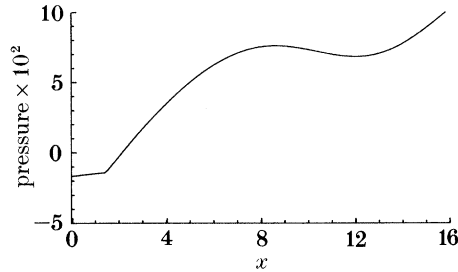


FIGURE 14. Computed pressure distribution along a free field computational boundary.

$y_{\max} = 14.0$ ,  $z = z_c = 7.0$  boundary is shown in figure 14 (the distributions along the other free field boundaries are similar). An abrupt change in the slope is apparent at  $x \approx 1.5$ . This corresponds to the approximate axial location at which the imposed deceleration of the free stream axial velocity begins (see §2.2). The pressure then increases linearly until the axial location corresponding to the maximum bubble diameter is reached. Downstream from this location the pressure decreases before increasing near the outflow. This behaviour is due to the influence the breakdown bubble has on the pressure field at the free field boundary. Experimental wall pressure distributions by Sarpkaya (1971*a*) in a tube-and-vane apparatus varied in a similar manner. Notice from the expanded scale in figure 14 that the maximum axial pressure variations along the free field boundary are about an order of magnitude smaller than the corresponding maximum variations along the vortex centreline.

The above discussion has been restricted to  $Re = 200$  calculations. Most practical applications occur at higher Reynolds numbers and it is of interest to determine what structural changes occur with increasing Reynolds numbers. We have made preliminary calculations at a Reynolds number of 1000, with all other parameters being identical to those discussed previously. At this higher Reynolds number we consider the grid resolution to be inadequate. Attempts to increase the resolution in the region of the bubble through grid-stretching were not successful, due to the overly large aspect ratio of the resulting cells. In any event, a brief discussion of the qualitative results may be useful. The most dramatic change is that the time required for the breakdown bubble to form decreased by about 30%. This supports the notion that the breakdown mechanism is inviscid in nature. The internal structure and aspect ratio of the bubble remain qualitatively similar. For instance, the quiescent region in the front of the bubble persists, as does the major recirculation region in the aft portion. A contrasting feature is that the radius of the bubble has decreased by approximately 20%. Future studies are anticipated which may address the high-Reynolds-number issue in greater detail.

In addition, a preliminary study regarding the period of the dominant axial velocity fluctuations inside the aft section of the breakdown, at a Reynolds number of 200, was performed. The period turns out to be approximately 40 time units. This can be compared with the non-dimensional period of approximately 13 time units given by Faler & Leibovich (1978). We suspect the difference may be a result of the higher Reynolds number in the Faler & Leibovich study. This



conclusion is consistent with the comparatively rapid breakdown of the Reynolds number 1000 numerical results, although we were unable to carry out those calculations far enough in time to obtain the period. This limitation, again, results from our inability to adequately resolve the intense shear layers occurring at the higher Reynolds number.

#### 4. CONCLUDING REMARKS

Previous numerical solutions of vortex breakdown, using the axisymmetric Navier–Stokes equations, have produced results which were inconsistent with experimental observation. In this study a numerical simulation of an unconfined trailing wing-tip type vortex has been performed, which produces results that are obtained from a numerical solution of the full three-dimensional, unsteady, Navier–Stokes equations in vorticity–velocity variables. Unlike previous studies, there was no requirement of symmetry imposed on the flow field. The flow dynamics, which were parametrized in terms of the Rossby number and the Reynolds number, dictate the choice of freestream boundary conditions that allowed for the breakdown bubble to be positioned away from the computational boundaries and thus free from numerically induced constraints.

Consistent with experimental observations, the structure computed in the present study contained multiple internal cells, or ring vortices. In addition, the flow within the bubble was unsteady, asymmetric and dominated in the aft portion by large-amplitude velocity fluctuations. These fluctuations are responsible for the exchange of fluid between the bubble and the free stream. This is an important consideration for applications that depend on the structure of the breakdown bubble.

As the extensive mapping of the dynamic features in the vicinity of, and within, the breakdown bubble suggest, the present numerical approach can provide an insightful look into the spatial and temporal evolution of this type of vortex breakdown. Clearly, more detailed experiments can provide a better basis for both qualitative and quantitative comparisons with these numerical results and, possibly, suggest areas where more detailed numerical simulations are required. However, in the absence of such experiments, we believe that the present study has extended our knowledge of the structure and dynamics of these breakdown bubbles.

Extension of this work to the numerical simulation of other types of breakdown, specifically the spiral type, are currently underway.

Two of us (R. E. S., R. L. A.) acknowledge the partial support of NASA Langley Research Center through NASA grant NAG-1-530 and the Old Dominion University ICAM Fellowship Program. The authors thank Professor C. E. Grosch and Dr M. E. Rose for their helpful discussions.

## REFERENCES

- Batchelor, G. K. 1967 *An introduction to fluid dynamics*. Cambridge University Press.
- Benay, R. 1984 Numerical modeling of a vortex breakdown in a laminar flow of revolution. *Rech. Aerosp.* pp. 15–27.
- Benjamin, T. B. 1962 Theory of the vortex breakdown phenomena. *J. Fluid Mech.* **14**, 593–629.
- Bossell, H. H. 1969 Vortex breakdown flowfield. *Phys. Fluids* **12**, 498–508.
- Escudier, M. P. & Zehnder, N. 1982 Vortex-flow regimes. *J. Fluid Mech.* **115**, 105–121.
- Faler, J. H. & Leibovich, S. 1977 Disrupted states of vortex flow and vortex breakdown. *Phys. Fluids* **20**, 1385–1400.
- Faler, J. H. & Leibovich, S. 1978 An experimental map of the internal structure of a vortex breakdown. *J. Fluid Mech.* **86**, 313–335.
- Garg, A. K. & Leibovich, S. 1979 Spectral characteristics of vortex breakdown flowfields. *Phys. Fluids* **22**, 2053–2064.
- Gartshore, I. S. 1962 Recent work in swirling incompressible flow. *NRC Can. Aero. Rep.* LR-343.
- Gatski, T. B., Grosch, C. E. & Rose, M. E. 1989 The numerical solution of the Navier–Stokes equations for three-dimensional unsteady, incompressible flows by compact schemes. *J. comp. Phys.* **82**, 298–329.
- Grabowski, W. J. & Berger, S. A. 1976 Solutions of the Navier–Stokes equations for vortex breakdown. *J. Fluid Mech.* **75**, 525–544.
- Hafez, M., Kuruvila, G. & Salas, M. D. 1986 Numerical study of vortex breakdown. *AIAA 24th Aerospace Sciences Meeting, Reno, Nevada*. AIAA Paper no. 86-0558.
- Hall, M. G. 1967 A new approach to vortex breakdown. *Proc. Heat Transfer Fluid Mech. Inst. Stanford Univ. Press.*, pp. 319–340.
- Ito, T., Suematsu, Y. & Hayase, T. 1985 On the vortex breakdown phenomena in swirling pipe flow. *Mem. Faculty Engng, Nagoya Univ.* **37**, 117–178.
- Keller, H. B. 1970 A new difference scheme for parabolic problems. In *Numerical solutions of partial differential equation*, vol. 2. New York: Academic Press.
- Kopecky, R. M. & Torrance, K. E. 1973 Initiation and structure of axisymmetric eddies in a rotating stream. *Computers Fluids* **1**, 289–300.
- Krause, E., Shi, X. & Hartwich, P. M. 1983 Computation of leading edge vortices. *AIAA Computational Fluid Dynamics Conf., Danvers, MA*. AIAA Paper no. 83-1907.
- Lavan, Z., Nielsen, H. & Fejer, A. A. 1969 Separation and flow reversal in swirling flows in circular ducts. *Phys. Fluids* **12**, 1747–1757.
- Leibovich, S. 1978 The structure of vortex breakdown. *A. Rev. Fluid Mech.* **10**, 221–246.
- Lugt, H. J. 1983 *Vortex flows in nature and technology*. New York: Wiley.
- Mager, A. 1972 Dissipation and breakdown of a wingtip vortex. *J. Fluid Mech.* **55**, 609–628.
- Narin, J. P. 1977 Numerical prediction of confined swirling jets. *Computers Fluids* **5**, 115–125.
- Randall, J. D. & Leibovich, S. 1973 The critical state: a trapped wave model of vortex breakdown. *J. Fluid Mech.* **53**, 495–515.
- Sarpkaya, T. 1971a On stationary and traveling vortex breakdown. *J. Fluid Mech.* **45**, 545–559.
- Sarpkaya, T. 1971b Vortex breakdown in swirling conical flows. *AIAA J.* **9**, 1792–1799.
- Sarpkaya, T. 1974 Effect of adverse pressure gradient on vortex breakdown. *AIAA J.* **12**, 602–607.
- Singh, P. I. & Uberoi, M. S. 1976 Experiments on vortex stability. *Phys. Fluids* **19**, 1858–1863.
- Spall, R. E. & Gatski, T. B. 1987 A numerical simulation of vortex breakdown. *Forum on unsteady flow separation* (ed. K. N. Ghia). *ASME appl. Mech., Bioengineering and Fluids Engineering Conf., Cincinnati, OH*. FED, vol. 52, pp. 25–33.
- Spall, R. E., Gatski, T. B. & Grosch, C. E. 1987 A criterion for vortex breakdown. *Phys. Fluids* **30**, 3434–3440.
- Squire, H. B. 1960 Analysis of the ‘vortex breakdown’ phenomenon. Part I. Aero. Dept. Imperial Coll. London, Rep. 102.
- Stuart, J. T. 1987 A critical review of vortex-breakdown theory. *Proc. Symp. Vortex Control and Breakdown Behavior, Baden, Switzerland*.

- Syred, N. & Beer, J. M. 1974 Combustion in swirling flows: a review. *Combustion Flame* **23**, 143–201.
- Uchida, S., Nakamura, Y. & Ohsawa, M. 1985 Experiments on the axisymmetric vortex breakdown in a swirling air flow. *Trans. Japan Soc. Aero. Sci.* **27**, 206–216.
- Wu, J. C. 1984 Fundamental solutions and numerical methods for flow problems. *Int. J. Num. Methods Fluids* **4**, 185–201.

Colour plate printed by George Over Limited, Rugby, U.K.